

Protocols to measure the non-Abelian Berry phase by pumping a spin qubit through a quantum-dot loop

Baksa Kolok^{1,*} and András Pályi^{1,2,†}

¹*Department of Theoretical Physics, Institute of Physics,*

Budapest University of Technology and Economics, Műegyetem rkp. 3., H-1111 Budapest, Hungary

²*MTA-BME Quantum Dynamics and Correlations Research Group, Műegyetem rkp. 3., H-1111 Budapest, Hungary*

(Dated: August 11, 2023)

A quantum system constrained to a degenerate energy eigenspace can undergo a nontrivial time evolution upon adiabatic driving, described by a non-Abelian Berry phase. This type of dynamics may provide logical gates in quantum computing that are robust against timing errors. A strong candidate to realize such holonomic quantum gates is an electron or hole spin qubit trapped in a spin-orbit-coupled semiconductor, whose twofold Kramers degeneracy is protected by time-reversal symmetry. Here, we propose and quantitatively analyze protocols to measure the non-Abelian Berry phase by pumping a spin qubit through a loop of quantum dots. One of these protocols allows to characterize the local internal Zeeman field directions in the dots of the loop. We expect a near-term realisation of these protocols, as all key elements have been already demonstrated in spin-qubit experiments. These experiments would be important to assess the potential of holonomic quantum gates for spin-based quantum information processing.

I. INTRODUCTION

Recent demonstrations of coherent electron and hole spin control in semiconductor quantum dot arrays [1–6] represent milestones toward a fault-tolerant quantum processor of spin qubits. In such devices, spin-orbit interaction often plays an important role. For example, in the presence of a magnetic field, it enables resonant control of a spin qubit using an ac electric field [7–9].

In the absence of a magnetic field, spin-orbit coupling does not break the twofold Kramers degeneracy of a spin qubit. However, spin-orbit does trigger qubit dynamics in the presence of time-dependent electric fields via geometrical effects. On the one hand, if electric fields are intentionally used to move the qubit adiabatically along a closed loop in real space (such as in a loop of 3 quantum dots, as shown in Fig. 1a), then the qubit state undergoes a nontrivial time evolution in the two-dimensional Kramers-degenerate subspace, described by a path-dependent propagator that is often called the non-Abelian Berry phase [10–13]. Quantum gates based on such adiabatic control form the building blocks of holonomic quantum computing [14]. On the other hand, the same mechanism implies that the interplay of spin-orbit coupling and electrical fluctuations lead to geometrical qubit dephasing [12, 15]. To our knowledge, these geometrical effects predicted for spin-orbit-coupled particles have not yet been demonstrated experimentally.

The effect of the (Abelian) Berry phase [17] on non-degenerate levels has been observed in a variety of systems, from optical fibers [18] and semiconductor rings [19–21] to Bose condensates of ultracold atoms [22]. In addition, geometrical dephasing due to this Berry phase

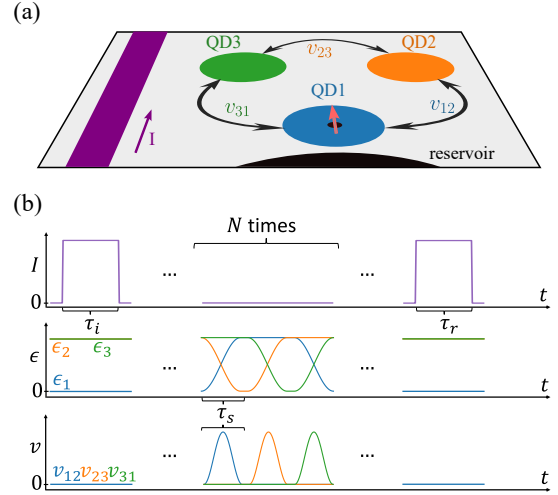


FIG. 1. Protocol to measure the non-Abelian Berry phase by adiabatically pumping a spin qubit through a quantum-dot (QD) loop. (a) Three QDs forming a loop. A reservoir resides next to QD1, enabling Elzerman-type readout [16]. A current (I) pulse through the wire (purple) induces magnetic field for initialisation and readout. (b) Current (I) and gate-voltage (ϵ , v) pulse sequence. Gate voltages control QD on-site energies (ϵ) and interdot tunneling energies (v). See Sec. VC for an alternative protocol that does not require pulsed magnetic fields, and relies on Pauli blockade for initialization and readout.

have been measured in superconducting qubits [23, 24].

As for the non-Abelian Berry phase, which is the focus of our work, experimental evidence has been observed in nuclear magnetic resonance experiments [25], and more recently in two-dimensional hole gases in semiconductors [26], in Bose condensates [27, 28], in coupled photonic waveguide structures [29] and in classical optical interfer-

* kolokba@edu.bme.hu

† palyi.andras@ttk.bme.hu

ence measurements using real space loops [30]. However, to our knowledge, the non-Abelian Berry phase has not been experimentally studied in quantum dot systems. In contrast to the recent experiments on non-Abelian Berry phases, where degeneracy of the system is achieved by fine tuning of the system's parameters [27–30], in a quantum dot system at zero magnetic field the energy degeneracy is due to time-reversal symmetry. It is reasonable to expect that this symmetry-based protection of the degeneracy is more robust than protection based on fine tuning. Hence, we consider spin qubits in the presence of spin-orbit coupling and absence of magnetic field as an outstanding experimental platform to measure non-Abelian Berry phase effects.

Here, we propose and theoretically analyse a protocol to measure the non-Abelian Berry phase by adiabatically pumping a spin qubit through a quantum-dot loop. Our main protocol, see Fig. 1, incorporates dc-pulsed magnetic fields for initialisation and readout, and qubit shuttling at zero magnetic field. We also propose a second version of the protocol to infer the key spin-orbit parameters of the multi-dot system, and a third version which uses Pauli-blockade initialisation and readout, and requires neither the magnetic field dc-pulse nor tunnelling to a reservoir. Furthermore, we describe variants for explicit demonstration of the non-Abelian (i.e., non-commutative) nature of the adiabatic geometric quantum gates. We anticipate that hole spin qubits in 2D arrays of Germanium quantum dots [1, 2, 31–33] are prominent candidates to carry out these experiments, due to their high device quality, planar 2D layout, strong spin-orbit interaction, and weak hyperfine effects. Note that single-electron shuttling experiments have been carried out in GaAs-based devices [34, 35]; however, there hyperfine interaction is comparatively strong, hindering spin qubit functionalities, and potentially masking the non-Abelian Berry phase effect.

The rest of the paper is organized as follows. In Sec. II, we present a minimal model describing the non-Abelian Berry phase propagator of a spin qubit as it is pumped through a quantum-dot loop. In Sec. III, we propose a measurement protocol to observe the non-Abelian Berry phase. In Sec. IV, we show that the interdot pseudospin-non-conserving tunneling parameters and the angles characterizing the local Zeeman fields can be inferred via a similar measurement protocol. We discuss an alternative protocol based on Pauli-blockade initialization and readout, as well as risks, challenges and further opportunities related to the proposed experiments, in Sec. V. We draw our conclusions in Sec. VI.

II. ADIABATIC CHARGE PUMPING THROUGH A QUANTUM DOT LOOP IN A MINIMAL MODEL

In this section, we introduce a minimal model to describe the non-Abelian Berry phase in a loop of three

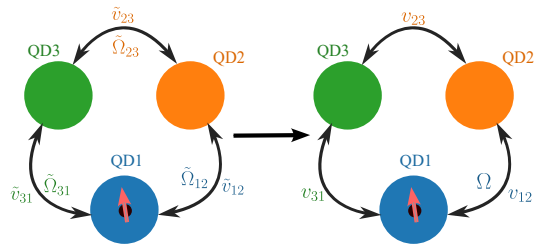


FIG. 2. A convenient gauge transformation for calculating the non-Abelian Berry phase. The pseudospin-non-conserving tunneling matrix elements between the dot pairs (QD2,QD3) and (QD3,QD1) are eliminated by the gauge transformation, which in turn transforms the pseudospin-non-conserving tunneling matrix elements between the dot pair (QD1,QD2) into Ω . By a further simultaneous pseudospin rotation on all three dots, $\Omega = \Omega(0, 0, 1)$ can be achieved.

quantum dots.

A. Setup, model, and the non-Abelian Berry phase

Consider a particle (an electron or a hole) in a quantum dot loop, subject to spin-orbit interaction. The setup is shown in Fig. 1a. Assume that the qubit is initialized in a specific state in the two-dimensional Kramers-degenerate subspace associated to the lowest-lying orbital of QD1. By slowly changing the plunger and barrier gate voltages, as depicted in Fig. 1b, the qubit is adiabatically pumped through the loop. As a result of being moved in the presence of spin-orbit interaction, the qubit state is rotated by the end of a full cycle. This qubit rotation can be phrased in terms of a non-Abelian Berry phase, which we describe as follows.

We take into account the ground-state orbitals of each QD, and the corresponding Kramers doublets which we call pseudospin doublets. Hence, with three dots, the Hilbert space is six dimensional. As long as we work with arbitrary pseudospin basis states, the model Hamiltonian of this setup reads

$$H = H_{\text{on-site}} + H_{\text{tun}} + H_{\text{stun}}, \quad (1a)$$

$$H_{\text{on-site}} = \epsilon_1 \tau_1 + \epsilon_2 \tau_2 + \epsilon_3 \tau_3, \quad (1b)$$

$$H_{\text{tun}} = \tilde{v}_{12} \tau_{12}^x + \tilde{v}_{23} \tau_{23}^x + \tilde{v}_{31} \tau_{31}^x, \quad (1c)$$

$$H_{\text{stun}} = \hbar \tilde{\Omega}_{12} \cdot \tilde{\sigma} \otimes \tau_{12}^y + \hbar \tilde{\Omega}_{23} \cdot \tilde{\sigma} \otimes \tau_{23}^y + \hbar \tilde{\Omega}_{31} \cdot \tilde{\sigma} \otimes \tau_{31}^y, \quad (1d)$$

where $\tilde{\sigma}_\alpha$ is the α -th Pauli operator acting on the pseudospin degree of freedom for $\alpha \in \{x, y, z\}$, $\tilde{\sigma}$ is the vector of $\tilde{\sigma}_\alpha$, τ_k with $k \in \{1, 2, 3\}$ is the projection on the k -th dot, and τ_{jk}^α with $j, k \in \{1, 2, 3\}$ is the Pauli α operator between the dots j and k .

The matrix forms of these operators can be expressed using the basis vectors representing wave functions localized on quantum dot k . These basis vectors are denoted as $|k, \downarrow\rangle$ and $|k, \uparrow\rangle$, and they are assumed to be

Kramers pairs, i.e., $|k, \tilde{\downarrow}\rangle = \mathcal{T}|k, \tilde{\uparrow}\rangle$ with \mathcal{T} being the time-reversal operator. The operators in Eq. (1) read, for example, as $\tau_k = |k, \tilde{\downarrow}\rangle \langle k, \tilde{\downarrow}| + |k, \tilde{\uparrow}\rangle \langle k, \tilde{\uparrow}|$, $\tau_{jk}^x = |j\rangle \langle k| + |k\rangle \langle j|$ and $\tau_{jk}^y = -i|j\rangle \langle k| + i|k\rangle \langle j|$. Tunneling between the j -th and the k -th dot is described by four parameters: \tilde{v}_{jk} is the pseudospin-conserving tunneling, and $\tilde{\Omega}_{jk}$ is the vector describing the pseudospin-non-conserving tunneling. The pseudospin-non-conserving tunneling terms in the Hamiltonian are induced by spin-orbit coupling [36].

Since the Hamiltonian H describes a single fermion in the presence of time-reversal symmetry (no magnetic field), the energy levels of H are twofold degenerate, known as Kramers degeneracy. Furthermore, the matrix form of the Hamiltonian depends on the choice of the localized basis vectors, which can be considered as a gauge degree of freedom. With an appropriate gauge transformation, we can simplify the Hamiltonian, as illustrated in Fig. 2: (i) Two of the three tunneling Hamiltonian terms, e.g., those between QD pairs (1,3) and (2,3), can be transformed to a pseudospin-conserving form. (ii) The pseudospin-non-conserving tunneling parameters of the third QD pair (1,2), obtained after this gauge transformation, form a vector with a single positive component, $\Omega = (0, 0, \Omega)$.

In fact, after this gauge transformation, the tunneling terms H_{tun} and H_{stun} transform into the following form:

$$H_{\text{tun}} = v_{12}\tau_{12}^x + v_{23}\tau_{23}^x + v_{31}\tau_{31}^x, \quad (2a)$$

$$H_{\text{stun}} = \hbar\Omega\sigma_z \otimes \tau_{12}^y. \quad (2b)$$

The parameters of these terms can be expressed with the old parameters, see App. A for the formulas and the detailed derivation. The Pauli matrices in Eq. (2) are expressed in the new basis, denoted as $|k, \tilde{\downarrow}\rangle, |k, \tilde{\uparrow}\rangle$. Note that the above gauge specification still leaves a gauge freedom, in the sense that a further global pseudospin rotation around the z axis leaves the Hamiltonian unchanged.

In our chosen gauge, the unitary qubit propagator U (a.k.a. ‘the non-Abelian Berry phase’ or a ‘holonomic quantum gate’) corresponding to a full adiabatic pumping cycle QD1 \rightarrow QD2 \rightarrow QD3 \rightarrow QD1 of the qubit through the loop reads

$$U = \frac{1}{\sqrt{v_{12}^2 + \hbar^2\Omega^2}} \begin{pmatrix} v_{12} + i\hbar\Omega & 0 \\ 0 & v_{12} - i\hbar\Omega \end{pmatrix} = e^{i\frac{\theta_{\text{so}}}{2}\sigma_z}, \quad (3)$$

where $\theta_{\text{so}} = 2 \arctan\left(\frac{\hbar\Omega}{v_{12}}\right)$, and the basis ordering is $|1, \tilde{\uparrow}\rangle, |1, \tilde{\downarrow}\rangle$. This unitary U is a pseudospin rotation around the z axis with angle θ_{so} . We provide the derivation of this result in the next subsection.

B. Derivation of Eq. (3)

The propagator U_{cycle} describing the time evolution of the qubit through the complete adiabatic cycle QD1 \rightarrow QD2 \rightarrow QD3 \rightarrow QD1 is a 6×6 matrix, which can be represented with the basis ordering $|1, \tilde{\uparrow}\rangle, |1, \tilde{\downarrow}\rangle, |2, \tilde{\uparrow}\rangle, \dots, |3, \tilde{\downarrow}\rangle$. This cycle propagator can be expressed using the 6×6 propagators W_{21} , W_{32} and W_{13} of each tunneling step as

$$U_{\text{cycle}} = W_{13}W_{32}W_{21}. \quad (4)$$

We calculate the propagator W_{21} , which corresponds to the first shuttling step, using the block-diagonal unitary transformation $V = \text{diag}(I, U^\dagger, I)$, where U is the unitary defined in Eq. (3). This transformation of the Hamiltonian renders the tunneling between QD1 and QD2 pseudospin-conserving. Although this transformation renders the tunneling between QD2 and QD3 pseudospin-non-conserving, this does not complicate the calculation as tunneling between QD2 and QD3 is suppressed in this shuttling step (see Fig. 1b, showing that the supports of $v_{12}(t)$ and $v_{23}(t)$ are disjoint). Thus, the transformed Hamiltonian is trivial for the pseudospin degree of freedom.

Together with the adiabatic nature of the tunneling dynamics, these imply that the propagator for the first tunneling step has the following block-matrix form:

$$\tilde{W}_{21} = \begin{pmatrix} 0 & e^{-i\phi_{21}^+} & 0 \\ e^{-i\phi_{21}^-} & 0 & 0 \\ 0 & 0 & e^{-i\epsilon_3\tau_s} \end{pmatrix}. \quad (5)$$

Here, ϕ_{21}^\pm are dynamical phases depending on the actual pulse shapes and timings, and τ_s is the time of the shuttling. Transforming this propagator back, we obtain:

$$W_{21} = V^\dagger \tilde{W}_{21} V = \begin{pmatrix} 0 & e^{-i\phi_{21}^+} U^\dagger & 0 \\ e^{-i\phi_{21}^-} U & 0 & 0 \\ 0 & 0 & e^{-i\epsilon_3\tau_s} \end{pmatrix}. \quad (6)$$

For the other two shuttling steps, the tunneling is pseudospin-conserving, therefore the propagators have the following form:

$$W_{32} = \begin{pmatrix} e^{-i\epsilon_1\tau_s} & 0 & 0 \\ 0 & 0 & e^{-i\phi_{32}^+} \\ 0 & e^{-i\phi_{32}^-} & 0 \end{pmatrix}, \quad (7a)$$

$$W_{13} = \begin{pmatrix} 0 & 0 & e^{-i\phi_{13}^-} \\ 0 & e^{-i\epsilon_2\tau_s} & 0 \\ e^{-i\phi_{13}^+} & 0 & 0 \end{pmatrix}, \quad (7b)$$

where ϕ_{32}^\pm and ϕ_{13}^\pm are dynamical phases.

Multiplying together the three propagators as in Eq. (4), we arrive to the cycle propagator that reads

$$U_{\text{cycle}} = \begin{pmatrix} e^{-i\phi_1} U & 0 & 0 \\ 0 & 0 & e^{-i\phi_2} \\ 0 & e^{-i\phi_3} U^\dagger & 0 \end{pmatrix}. \quad (8)$$

Here, the phases are dynamical and could be expressed from the dynamical phases described above. As long as the qubit is localized on the first dot at the start of the process, the relevant part of U_{cycle} is its top left 2×2 block with U being defined in Eq. (3), and the dynamical phases have no physical significance.

III. MEASUREMENT PROTOCOL FOR THE NON-ABELIAN BERRY PHASE

In the previous section, we derived a formula, Eq. (3), for the non-Abelian Berry phase that characterizes an adiabatic pumping cycle of a single particle in a loop of three quantum dots. In general, the non-Abelian Berry phase of such a spin- $\frac{1}{2}$ particle is a 2×2 unitary transformation. This unitary transformation corresponds to a rotation on the Bloch-sphere, therefore it can be described with an angle and an axis.

In this section, we propose a measurement to determine the angle and the axis corresponding to the non-Abelian Berry phase induced by an adiabatic pumping cycle in the quantum dot loop. In fact, the angle is a gauge-invariant physical quantity. The axis, however, is a gauge-dependent quantity; below we describe how the axis is characterized by our measurement protocol.

We consider a single particle in the three-dot loop as described above, and shown in Fig. 1a. The setup includes a metallic wire (purple stripe in Fig. 1a) that can host current dc pulses (purple solid line in Fig. 1b), and a particle reservoir (black in Fig. 1a) that is used for Elzerman-type qubit readout[16].

The protocol starts with having a single particle in QD1, and having no particles in QD2 and QD3. As the first step, a current dc pulse is applied on the wire, to produce a dc magnetic field pulse that is felt by the particle in QD1 [37, 38]. The duration of the dc pulse is long enough such that the pseudospin of the particle in QD1 can thermalize, i.e., the pseudospin is initialised with a sufficiently high fidelity. After switching off the current (and hence the magnetic field), the particle is adiabatically pumped through the loop via the sequence QD1 \rightarrow QD2 \rightarrow QD3 \rightarrow QD1, to induce the non-Abelian Berry phase. This step might be repeated N times, which amounts to performing the same geometric gate N times. Finally, the qubit is read out in QD1 by Elzerman readout, utilizing a second current dc pulse.

Let us denote the probability of reading out the qubit in its excited state after the N th cycle as $P_{1,e,N}^{(m)}$. Below, we argue that the angle and the axis of the non-Abelian Berry phase can be characterized from the experimental data of this readout probability $P_{1,e,N}^{(m)}$.

For this analysis, we first describe the time duration over which the initial current dc pulse is switched on, creating a magnetic field \mathbf{B} . For simplicity, we assume that this magnetic field is homogeneous over the volume of QD1. The Zeeman term induced by the magnetic field, expressed in the same general gauge as used in Eq. (1a),

takes the following form:

$$H_{\text{Zeeman}} = \sum_{k=1}^3 \frac{1}{2} \mu_B \tilde{\boldsymbol{\sigma}} \cdot \tilde{\mathbf{g}}_k \mathbf{B} \otimes \tau_k, \quad (9)$$

where $\tilde{\mathbf{g}}_k$ is the g -tensor of the k -th dot (a real, not necessarily symmetric 3×3 matrix), and μ_B is the Bohr magneton. We also introduce the notion of the local Zeeman vectors: $\hbar \tilde{\boldsymbol{\omega}}_k = \mu_B \tilde{\mathbf{g}}_k \mathbf{B}$.

Let us transform the Hamiltonian H , which is now supplemented by the Zeeman term H_{Zeeman} , to the same gauge as it is in Eqs. (2a) and (2b). This means a rotation of the g -tensors (see App. B for details). As it was mentioned before, the gauge specification in Sec. II A still leaves a residual gauge freedom, i.e., we can further specify the gauge with a global pseudospin rotation that affects the Zeeman term only but leaves the other three terms in H invariant. With the appropriate choice of the rotation, we rotate the local Zeeman vector of the first dot into the xz plane with $x > 0$. Effectively, this rotation transforms the g -tensors of the Zeeman term.

We denote the g -tensors after the transformations as \mathbf{g}_k . Then, the Hamiltonian of the system in that gauge is the following:

$$H = H_{\text{on-site}} + H_{\text{tun}} + H_{\text{stun}} + H_{\text{Zeeman}}, \quad (10a)$$

$$H_{\text{on-site}} = \epsilon_1 \tau_1 + \epsilon_2 \tau_2 + \epsilon_3 \tau_3, \quad (10b)$$

$$H_{\text{tun}} = v_{12} \tau_{12}^x + v_{23} \tau_{23}^x + v_{31} \tau_{31}^x, \quad (10c)$$

$$H_{\text{stun}} = \hbar \Omega \sigma_z \otimes \tau_{12}^y, \quad (10d)$$

$$H_{\text{Zeeman}} = \frac{1}{2} \mu_B B \sum_{k=1}^3 g_k (\mathbf{n}_k \cdot \boldsymbol{\sigma}) \otimes \tau_k. \quad (10e)$$

where $g_k = \frac{|\mathbf{g}_k \mathbf{B}|}{B}$ is the g -factor of the k -th dot corresponding to the given direction of the magnetic field and $\mathbf{n}_k = (\sin \theta_k \cos \phi_k, \sin \theta_k \sin \phi_k, \cos \theta_k) = \frac{\mathbf{g}_k \mathbf{B}}{g_k B}$ is the unit vector in the direction of the local Zeeman field on the k -th dot. Moreover, $\phi_1 = 0$, because, as we mentioned above, the local Zeeman vector in QD1 is in the xz plane with $x > 0$.

The qubit ground state and excited state in QD1 are expressed in the basis $|1, \uparrow\rangle, |1, \downarrow\rangle$ as

$$|1, g\rangle = \begin{pmatrix} \sin\left(\frac{\theta_1}{2}\right) \\ -\cos\left(\frac{\theta_1}{2}\right) \end{pmatrix}, \quad |1, e\rangle = \begin{pmatrix} \cos\left(\frac{\theta_1}{2}\right) \\ \sin\left(\frac{\theta_1}{2}\right) \end{pmatrix}. \quad (11)$$

Therefore, the thermal equilibrium state of the system after the initialisation is

$$\rho_1 = \frac{1}{1 + e^{-\frac{\hbar \omega_1}{k_B T}}} \left(|1, g\rangle \langle 1, g| + e^{-\frac{\hbar \omega_1}{k_B T}} |1, e\rangle \langle 1, e| \right), \quad (12)$$

with $\omega_k = |\tilde{\boldsymbol{\omega}}_k|$. After N pumping cycles, the pseudospin excited state occupation in QD1 yields:

$$P_{1,e,N} = \langle 1, e | U_{\text{cycle}}^N \rho_1 U_{\text{cycle}}^{\dagger N} | 1, e \rangle = a(\theta_1, T, \omega_1) - b(\theta_1, T, \omega_1) \cos(N\theta_{\text{so}}) \quad (13)$$

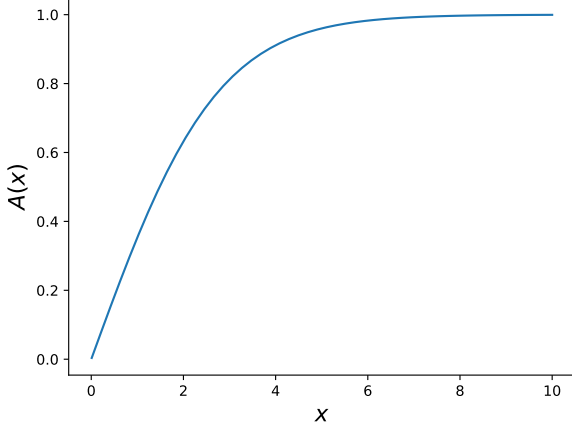


FIG. 3. The function $A(x)$ defined in Eq. (16b), which reduces the signal contrast due to the readout error caused by the thermal broadening of Fermi-Dirac distribution of particles in the reservoir.

where $\theta_{\text{so}} = 2 \arctan\left(\frac{\hbar\Omega}{v_{12}}\right)$, and we introduced the following quantities:

$$a(\theta_1, T, \omega_1) = \frac{1}{2} - \frac{\tanh\left(\frac{\hbar\omega_1}{k_B T}\right) \cos^2 \theta_1}{2}, \quad (14a)$$

$$b(\theta_1, T, \omega_1) = \frac{\tanh\left(\frac{\hbar\omega_1}{k_B T}\right) \sin^2 \theta_1}{2}. \quad (14b)$$

However, due to the finite temperature of the reservoir, the Elzerman-type readout does not yield the occupation probabilities. The actual measurement outcome ($P_{1,e,N}^{(m)}$) has the same form as (13) but with modified parameters:

$$P_{1,e,N}^{(m)} = a^{(m)}(\theta_1, T, \omega_1) - b^{(m)}(\theta_1, T, \omega_1) \cos(N\theta_{\text{so}}). \quad (15)$$

This means that the contrast of the oscillating signal is reduced as

$$b^{(m)}(\theta_1, T, \omega_1) = A\left(\frac{\hbar\omega_1}{2k_B T}\right) \frac{\tanh\left(\frac{\hbar\omega_1}{k_B T}\right) \sin^2 \theta_1}{2}, \quad (16a)$$

$$A(x) = \exp\left(\frac{x}{1-e^x}\right) - \exp\left(\frac{x}{e^{-x}-1}\right). \quad (16b)$$

We illustrated the function $A(x)$ in Fig. 3 to show how the signal contrast is modified if the Zeeman splitting is comparable to the temperature of the reservoir. For a detailed description and derivation of Eq. (16) see App. C.

Equation (15) is the central result of this work. It is an approximate result, valid in the adiabatic limit. To illustrate its relation to experiments, where the adiabatic

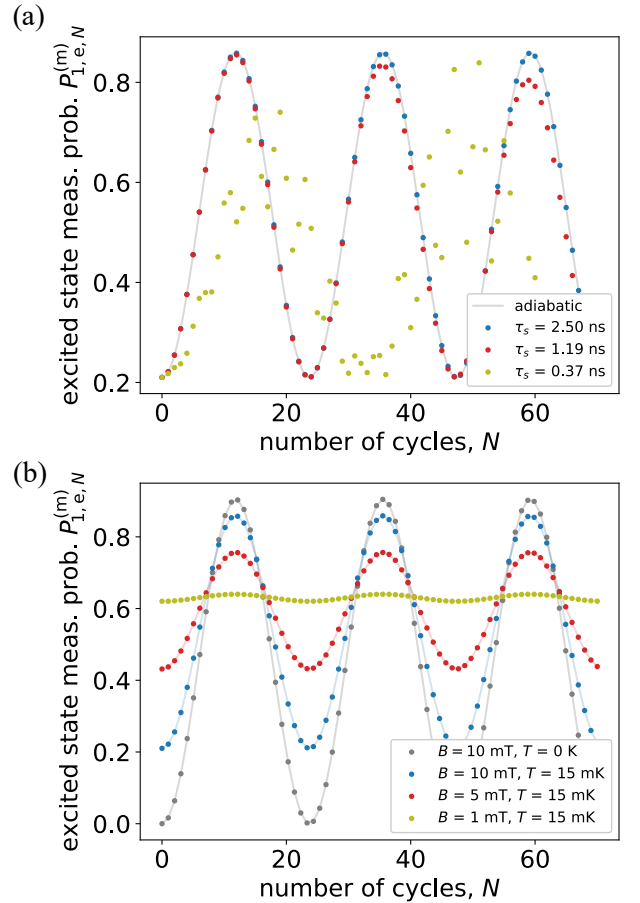


FIG. 4. Effect of the non-Abelian Berry phase on pumping a spin-qubit through a quantum-dot loop. (a) Simulation results of the measured excited state probability after N pumping cycles. Gray solid line shows the result obtained from ideal adiabatic evolution, Eq. (15). Further data sets correspond to different shuttling times, see inset. For slow shuttling, $\tau_s = 2.5$ ns, the simulation result matches the solid analytical result. For faster braiding, $\tau_s \lesssim 2$ ns, the evolution is not adiabatic anymore. Parameters: $\epsilon_k = 30 \mu\text{eV}$, $v_{12} = 30 \mu\text{eV}$, $v_{23} = 28 \mu\text{eV}$, $v_{31} = 32 \mu\text{eV}$, $\hbar\Omega = 4 \mu\text{eV}$, $T = 15 \text{ mK}$, $B = 10 \text{ mT}$, $g_1 = 11$, $\theta_1 = 72^\circ$, where the parameters ϵ_k and v_{jk} are the amplitudes of the applied signals for the shuttling pulses shown in Fig. 1b. Pulse shapes are sine for ϵ_k -s and sine-squared for v_{jk} -s. (b) Analytical result Eq. (15) for the measured excited state probability for different magnetic field strengths used for the initialisation and different temperatures. Parameters as above. Gray solid line is the ideal case when $T = 0 \text{ K}$, i.e., when initialisation and readout are perfect.

approximation might break down, in Fig. 4a we show simulation results obtained by solving the time-dependent Schrödinger equation numerically. Blue, red and yellow data points show simulated results for three different shuttling times (see inset), whereas the solid line shows the adiabatic result of Eq. (15). First, the solid line and the blue data points match to a high degree, confirming

the analytical result Eq. (15). Second, as the shuttling time is decreased ($\tau_s \lesssim 2$ ns), the mismatch with the adiabatic result grows significantly. We attribute the irregularities developing for shorter shuttling times to diabatic transitions during the shuttling dynamics.

In Fig. 4b, we illustrate the importance of the relative strength of the Zeeman splitting used to initialise the qubit and thermal fluctuations, focusing on the adiabatic limit for simplicity. Fig. 4b shows that increasing the Zeeman splitting at a fixed temperature leads to an enhanced contrast of the oscillations, i.e., for a clear illustration of the effect it is beneficial to increase the dc magnetic-field pulse strength and decrease the temperature as much as possible.

The above theory analysis defines an experimental protocol to infer the angle θ_{so} of the single-cycle non-Abelian Berry phase and the angle θ_1 . For each N , the sequence ‘initialization \rightarrow adiabatic cyclic pumping N times \rightarrow readout’ should be repeated many times to obtain the probability data points similar to those in Fig. 4. Those probabilities should then be fitted with a harmonic function of the form (15) to extract the angle θ_{so} of the single-cycle non-Abelian Berry phase. If the temperature T and the Larmor frequency ω_1 are known, then the only fit parameters are θ_{so} and θ_1 .

We emphasize here, that we have outlined this procedure in terms of a specific minimal model, but the procedure is more general. In any model describing a quantum dot loop, the non-Abelian Berry phase can be described as a rotation (of angle θ_{so}) on the Bloch-sphere, and the magnetic field used for initialisation and readout defines a Kramers basis to which the axis of the rotation can be compared (θ_1).

IV. MEASUREMENT PROTOCOL FOR THE INTERNAL ZEEMAN FIELD DIRECTIONS

A small variation of the previous protocol gives a technique to parametrize the local Zeeman field directions θ_2 and ϕ_2 in QD2, as well as θ_3 and ϕ_3 in QD3. The setup is the same as before (Fig. 1a), but this protocol uses two further variants of the initialisation, as shown in Fig. 5. These variants differ in the location of the particle during the initializing magnetic-field pulse. After that pulse, the particle is adiabatically pumped, counterclockwise, to QD1.

Each of these three different preparation procedures results in a different pseudospin state located in QD1, with the pseudospin state depending on the local Zeeman field direction of the QD where the particle was initialized. Then, the protocol is continued the same way as in the previous section, i.e., N adiabatic pumping cycles in the loop and then the pseudospin measurement in QD1. From the measurement data obtained this way, the angles $\theta_2, \phi_2, \theta_3, \phi_3$ describing the local Zeeman field directions in the specific gauge can be inferred. This provides a full characterisation of our minimal model described in

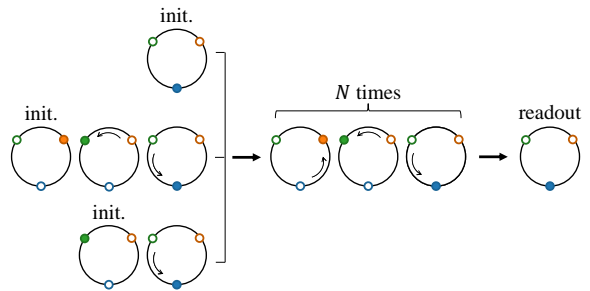


FIG. 5. Protocol to infer local Zeeman field directions on the quantum dot of the loop. Three preparation procedures (left) are distinguished. Particle position (filled circle) is shown at the subsequent steps of the protocol. Initialisation (‘init.’) is done when the particle is localized in one of the dots. Then the particle is shuttled counterclockwise to QD1. After N adiabatic pumping cycles, readout is done in QD1.

Sec. II A.

Although we have described this protocol using a minimal model, we note that the goal of this protocol and the protocol itself generalises naturally to any model describing adiabatic pumping through a quantum-dot loop. In such a generalised model, the angle parameters ϕ_k and θ_k can still be defined as the directions of the local Zeeman fields in the dots in a gauge, where pseudospin is conserved upon tunneling between pairs QD3 \leftrightarrow QD1 and QD2 \leftrightarrow QD3.

To analyse the protocol, let us fix the same gauge as before in Eq. (10), i.e., interdot tunneling is pseudospin conserving everywhere except between QD1 and QD2, where it is described by the vector Ω pointing in the z direction. The Zeeman field direction in the k -th dot is described with two angles θ_k, ϕ_k and we further assume that $\phi_1 = 0$.

In this gauge, the ground state and the excited state can be expressed in the $|k, \uparrow\rangle, |k, \downarrow\rangle$ basis, when the particle is localized in the k -th dot, and the magnetic field is switched on:

$$|k, g\rangle = \begin{pmatrix} \sin\left(\frac{\theta_k}{2}\right) \\ -e^{i\phi_k} \cos\left(\frac{\theta_k}{2}\right) \end{pmatrix}, \quad |k, e\rangle = \begin{pmatrix} e^{-i\phi_k} \cos\left(\frac{\theta_k}{2}\right) \\ \sin\left(\frac{\theta_k}{2}\right) \end{pmatrix}. \quad (17)$$

Thus, after thermalisation, the system is in the following state:

$$\tilde{\rho}_k = \frac{1}{1 + e^{-\frac{\hbar\omega_k}{k_B T}}} \left(|k, g\rangle \langle k, g| + e^{-\frac{\hbar\omega_k}{k_B T}} |k, e\rangle \langle k, e| \right). \quad (18)$$

The thermalisation is followed by counterclockwise adiabatic shuttling of the particle to QD1 (e.g., from QD2, on the route QD2 \rightarrow QD3 \rightarrow QD1), where the tunneling is pseudospin-conserving. Therefore, the state $|k, g\rangle$ ($|k, e\rangle$) evolves to the state

$$|g_k\rangle = \sin\left(\frac{\theta_k}{2}\right) |1, \uparrow\rangle - e^{i\phi_k} \cos\left(\frac{\theta_k}{2}\right) |1, \downarrow\rangle, \quad (19)$$

(analogous formula for $|e_k\rangle$), which has the same amplitudes as $|k, g\rangle$ in Eq. (18) ($|k, e\rangle$), but is expressed in the basis $|1, \uparrow\rangle, |1, \downarrow\rangle$ localized in QD1. As a consequence, the state of the system after this preparation procedure reads:

$$\rho_k = \frac{1}{1 + e^{-\frac{\hbar\omega_k}{k_B T}}} \left(|g_k\rangle \langle g_k| + e^{-\frac{\hbar\omega_k}{k_B T}} |e_k\rangle \langle e_k| \right). \quad (20)$$

The next step is to adiabatically pump the particle through the loop N times. The probability of the excited state occupation in QD1 after N cycles reads:

$$\begin{aligned} P_{k,e,N} &= \langle 1, e | U_{\text{cycle}}^N \rho_k U_{\text{cycle}}^{\dagger N} | 1, e \rangle = \\ &= a_k - b_k \cos(N\theta_{\text{so}} - \phi_k), \end{aligned} \quad (21)$$

where $\theta_{\text{so}} = 2 \arctan\left(\frac{\hbar\Omega}{v_{12}}\right)$, as before, and we introduced the parameters:

$$a_k(\theta_k, \theta_1, T, \omega_k) = \frac{1}{2} - \frac{\tanh\left(\frac{\hbar\omega_k}{2k_B T}\right) \cos\theta_1 \cos\theta_k}{2}, \quad (22a)$$

$$b_k(\theta_k, \theta_1, T, \omega_k) = \frac{\tanh\left(\frac{\hbar\omega_k}{2k_B T}\right) \sin\theta_1 \sin\theta_k}{2}. \quad (22b)$$

As a refinement of this result, we consider the same type of readout error as in the previous section. This implies that the oscillation contrast of the measured excited-state probability $P_{k,e,N}^{(m)}$ is reduced with respect to b_k in Eq. (22b) by the same thermal damping factor $A\left(\frac{\hbar\omega_1}{2k_B T}\right)$ as in Eq. (16a). We numerically simulated the resulting excited-state probabilities in the limit of adiabatic pumping, and show results in Fig. 6.

Using measurement data obtained via this protocol, one can infer the parameters of the model in Eq. (10). To this end, the measurement data obtained through the three variants (as shown in Fig. 6) is fitted simultaneously, e.g., using $\theta_{\text{so}}, \theta_1, \theta_2, \phi_2, \theta_3,$ and ϕ_3 as fit parameters, assuming that temperature T and Larmor frequencies ω_1, ω_2 and ω_3 are known. We note that θ_{so} is the only joint fit parameter of the three data sets, and it is the common ‘frequency’ characterising the oscillation of all $P_{k,e,N}^{(m)}$ as functions of N .

V. DISCUSSION

In this section, we discuss potential challenges and extensions of our proposed experimental protocol.

A. Optimizing the shuttling time: diabatic transitions, hyperfine interaction and charge noise

We expect that the experimental protocols we have proposed will work if the shuttling time is adjusted properly: It should neither be too fast, nor too slow. Too fast

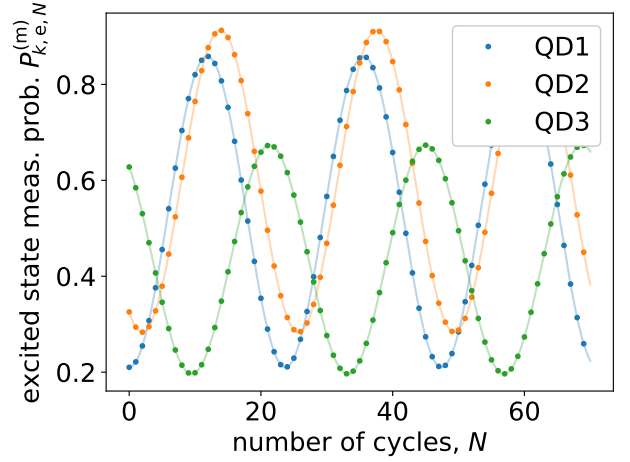


FIG. 6. The effect of the non-Abelian Berry phase depending on the qubit position during initialisation. Dots are simulation results, solid lines are analytical results of Eq. (15). Simulation shows agreement with the analytics. Parameters: $\tau_s = 2.5$ ns, $\epsilon_k = 30 \mu\text{eV}$, $v_{12} = 30 \mu\text{eV}$, $v_{23} = 28 \mu\text{eV}$, $v_{31} = 32 \mu\text{eV}$, $\hbar\Omega = 4 \mu\text{eV}$, $T = 15$ mK, $B = 10$ mT, $g_1 = 11$, $g_2 = 10.2$, $g_3 = 15$, $\theta_1 = 72^\circ$, $\phi_1 = 0^\circ$, $\theta_2 = 102.9^\circ$, $\phi_2 = 30^\circ$, $\theta_3 = 36^\circ$, $\phi_3 = 144^\circ$, where the parameters ϵ_k and v_{jk} are the amplitudes of the applied sine and sine-squared of sine pulses for the shuttlings shown in Fig. 1b.

shuttling leads to diabatic transitions, leading to errors, such as those exemplified in Fig. 4a. Too slow shuttling enables qubit decoherence due to various noise types.

We estimate a lower bound on the shuttling time using the Landau-Zener description for the diabatic transition in a two-level system with Hamiltonian:

$$H = \begin{pmatrix} \frac{\delta\epsilon(t)}{2} & v \\ v & -\frac{\delta\epsilon(t)}{2} \end{pmatrix}, \quad (23)$$

where $\delta\epsilon(t) = \alpha t$. In the Landau-Zener setup, dynamics starts in the ground state at $t = -\infty$ and ends at $t = \infty$. The diabatic transition probability (P_d) is given by the Landau-Zener formula [39]:

$$P_t = e^{-\frac{v^2}{\hbar\alpha}}, \quad (24)$$

To describe the dynamics in our shuttling setup, we estimate the sweep velocity as $\alpha = \frac{\epsilon\pi}{\tau_s}$. Substituting the realistic parameter values $\epsilon \approx v = 30 \mu\text{eV}$, for a $P_t < 10^{-4}$ suppression of the diabatic transition, we obtain the following constraint for the shuttling time:

$$\tau_s \gtrsim 4 \text{ ns}. \quad (25)$$

This order-of-magnitude estimate is in accordance with the simulation results in Fig. 4a.

We estimate an upper bound on the shuttling time by considering the effect of hyperfine interaction, caused by nuclear spins in the semiconductor hosting the quantum dots. Hyperfine interaction is an important and

well-described cause of dephasing in semiconductor spin qubits. Using a specific dephasing model [40], the qubit inhomogeneous dephasing time T_2^* caused by hyperfine interaction is expressed as:

$$\frac{\hbar^2}{T_2^{*2}} = \frac{1}{2N_n} \nu I(I+1) A_n^2, \quad (26)$$

where ν is the abundance of the isotope having nuclear spin I , $N_n = \pi a_B^{*2} w / v_0$ is the number of atoms in the quantum dot (a_B^* is the effective Bohr radius of the dot, w is the width of the quantum well, v_0 is the atomic volume of the host material), and A_n is the hyperfine interaction strength.

We estimate $T_2^* \approx 1.4 \mu\text{s}$ from Eq. (26), using realistic parameter values for holes in natural germanium [41]: $a_B^* = 50 \text{ nm}$, $w = 15 \text{ nm}$, $v_0 = 2.26 \cdot 10^{-2} \text{ nm}^3$, $\nu = 0.0776$, $I = 9/2$, and $A_n = -1.1 \mu\text{eV}$. This estimate indicates that an experiment with a few tens of cycles and a few-nanosecond shuttling time is feasible with hole spin qubits in natural Germanium. Motional narrowing [34, 35] and isotopic purification can further suppress effects of hyperfine interaction and hence increase this feasibility.

Charge noise, including fluctuating charge traps, gate-referred noise, and electron-phonon interaction, could also affect the feasibility of the experiment. For example, recent theoretical studies on spin-qubit shuttling [42, 43] did find that too slow shuttling suffers from errors caused by $1/f$ noise and phonons, and an optimal shuttling time $\tau_s \approx 5 \text{ ns}$ for tunneling amplitude $v = 30 \mu\text{eV}$ was estimated for electrons in Si and GaAs QDs. This time scale is the same order of magnitude as used in our simulations leading to Figs. 4 and 6.

Charge noise can also induce direct dephasing in zero magnetic field, called geometric dephasing [15]. The geometric dephasing time was estimated as $T_{\text{geom}} \approx 20 \text{ ms}$ for GaAs quantum dots at $T = 50 \text{ mK}$ in Ref. [15]. This suggests, that in our protocol the geometrical dephasing is negligible as compared to hyperfine noise.

To conclude, the time-scale estimates collected in this section suggest the feasibility of the experiments proposed in Sec. III and IV.

B. Risks and challenges

Earth's magnetic field. The Earth's magnetic field amounts to a few tens of microteslas. This may be regarded 'weak', but it is strong enough to affect the experiments proposed above. In fact, the Larmor precession time corresponding to a magnetic field of $B_E = 65 \mu\text{T}$ with g -factor $g = 2$ is $T_L \approx 550 \text{ ns}$. This Larmor time can be further shortened in materials with strong spin-orbit coupling, e.g., for planar hole quantum dots, where the g -factor is enhanced in an out-of-plane magnetic field. [2, 44, 45]. For shuttling times comparable to T_L , the non-Abelian adiabatic dynamics would be overwhelmed by the Larmor precession due to the magnetic field. The

effect can be reduced by using shorter shuttling times, e.g., in the few-nanosecond ballpark discussed above. To further mitigate this effect, the Earth's magnetic field should be shielded in the experiment, which can be done using well-established methods [46–49].

Coincidental alignment of the two axes ($\theta_1 = 0$). The key feature of the measurement results of the experimental protocol proposed in Sec. III is the oscillatory behavior of $P_{1,e,N}^{(m)}$ as the number N of cycles is increased, as shown in Eq. (15) and Fig. 4. From Eq. (16a), it is clear that this oscillatory behavior is absent if $\theta_1 = 0$. The success of the experiment proposed in Sec. III relies on the assumption that the Kramers basis $|1, g\rangle$, $|1, e\rangle$, defined by the local magnetic field used for initialization and readout, does *not* coincide with the Kramers eigenbasis $|1, \uparrow\rangle$, $|1, \downarrow\rangle$ of the non-Abelian Berry phase propagator. This is formalized as the assumption $\theta_1 \neq 0$. More generally, the relative angles θ_k play an important role in determining the contrast of the oscillations described by Eqs. (16a) and (22b). In an experiment, these angles, which are determined by the microscopic details of spin-orbit interaction, confinement and potentials, strain patterns, and disorder, can presumably be changed by continuous tuning of gate voltages, or by changing the charge occupations of the dots [2, 9, 50–52].

Efficient initialization and readout. As illustrated in Fig. 4(b), a strong magnetic field pulse and a low temperature are essential for high-fidelity initialization and readout, and consequently, for obtaining high-contrast excited-state probability oscillations in the experiment. A current pulse through an on-chip wire in the close vicinity of the quantum dot loop could deliver a millitesla-scale magnetic field [37], although its engineering and fabrication might be challenging. Therefore, to improve the visibility of the results one might need to cool the device below 15 mK (i.e., the value we have used in our simulations). Note that that the sub-millikelvin cooling of mesoscopic electronic devices is an active research area with recent successes [53–56]. Lower temperature has the additional advantage that it reduces the thermal excitation in the shuttling processes.

C. An alternative protocol without magnetic-field pulses: using the singlet state for initialisation and readout

In the previous section, we have discussed the challenges of creating a strong-enough magnetic-field pulse and a low-enough temperature for our experimental protocols. As a possible workaround of these, we now provide an alternative protocol, which requires an extra reference dot, denoted as QDR in Fig. 7, and utilizes a two-qubit singlet state in that reference dot for initialization and readout. This protocol can reveal the angle θ_{so} characterizing the non-Abelian Berry phase, without requiring a magnetic-field pulse. Furthermore, the low-temperature requirement is also relaxed, because ini-

tialization and readout is based on Pauli spin blockade, where the energy scale (the two-qubit singlet-triplet splitting in QDR) competing with temperature can be made much greater than the Zeeman splitting in a few millitesla [57].

The layout for this alternative protocol is shown in Fig. 7. To simplify the discussion, we use a specific gauge (i.e., specification of the Kramers-pair basis in the dots) where tunneling is pseudospin-conserving on the bonds QDR \leftrightarrow QD1, QD2 \leftrightarrow QD3, and QD3 \leftrightarrow QD1, and it is pseudospin-non-conserving only on the bond QD1 \leftrightarrow QD2. In this protocol, initialization consists of thermalizing a two-qubit singlet state in QDR, and separating the two particles with an adiabatic shuttling step, by tuning the detuning and tunneling between QDR and QD1 in time. Before (after) this shuttling, detuning favors the double occupancy of QDR (single occupancy of both QDR and QD1). Ideally, the tunneling matrix element v_{1R} is switched off exactly before and after the shuttling step. This initialization procedure results in the separated singlet configuration depicted in Fig. 7.

During a single pumping cycle QD1 \rightarrow QD2 \rightarrow QD3 \rightarrow QD1, the particle in QD1 is pumped around. Therefore, the time evolution of the two-qubit system is governed by the following unitary, expressed in the two-qubit basis $|\uparrow\uparrow\rangle, |\uparrow\downarrow\rangle, |\downarrow\uparrow\rangle, |\downarrow\downarrow\rangle$, with the first (second) arrow referring to QD1 (QDR):

$$V = \begin{pmatrix} e^{i\theta_{so}} & 0 & 0 & 0 \\ 0 & e^{i\theta_{so}} & 0 & 0 \\ 0 & 0 & e^{-i\theta_{so}} & 0 \\ 0 & 0 & 0 & e^{-i\theta_{so}} \end{pmatrix}. \quad (27)$$

Since the initial two-qubit state is the singlet state

$$|S\rangle = \frac{1}{\sqrt{2}} (|\uparrow\downarrow\rangle - |\downarrow\uparrow\rangle), \quad (28)$$

after N pumping cycles, it evolves into

$$\begin{aligned} V^N |S\rangle &= \frac{1}{\sqrt{2}} (e^{iN\theta_{so}} |\uparrow\downarrow\rangle - e^{-iN\theta_{so}} |\downarrow\uparrow\rangle) = \\ &= \cos(N\theta_{so}) |S\rangle + i \sin(N\theta_{so}) |T_0\rangle. \end{aligned} \quad (29)$$

At this point, the QDR and the single particle in it can be utilized once again, now for readout via spin-to-charge conversion based on Pauli blockade. Specifically, an attempt to shuttle the particle in QD1 to QDR is made, and charge sensing is done on the dots to reveal if the final state of QDR contains one or two particles. Due to Pauli blockade, one (two) particle(s) measured in QDR implies that the state $V^N |S\rangle$ was triplet (singlet). The singlet measurement probability is expressed from Eq. (29) as

$$P_S = |\langle S | V^N |S\rangle|^2 = \cos^2(N\theta_{so}). \quad (30)$$

The measurement data obtained for this singlet probability, as a function of the number N of the cycles, should

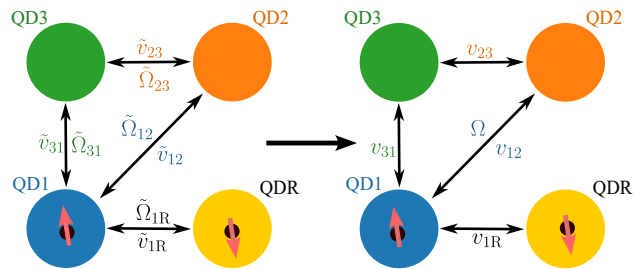


FIG. 7. Alternative protocol to measure the non-Abelian Berry phase using a reference dot and the Pauli blockade mechanism for initialization and readout. The advantage of this protocol is that direct dot-reservoir tunneling and magnetic-field pulses are not required. Initialization is done by separating a two-qubit singlet state in QDR into QDR and QD1; readout is done after N adiabatic pumping cycles QD1 \rightarrow QD2 \rightarrow QD3 \rightarrow QD1, by spin-to-charge conversion using Pauli blockade between QD1 and QDR. Left panel illustrates the tunneling terms of the Hamiltonian in an arbitrary gauge; right panel does the same in a convenient gauge where all tunneling terms are pseudospin-conserving, except the one on the QD1 \leftrightarrow QD2 bond.

show oscillations, whose ‘frequency’ reveals the angle of the non-Abelian Berry phase.

This protocol has advantages over the one described in Sec. III, which uses magnetic-field-enabled initialization and readout. First, no additional wire is required to create the magnetic-field pulse. Devices without that element are readily available in the 2×2 quantum dot array layout [1, 2, 31–33, 58]. Second, the oscillation of the measured singlet probability is not suppressed by the factor of $\sin^2 \theta_1$ (i.e., the angle between the axis of the non-Abelian Berry phase and the local Zeeman axis) appearing in Eq. (16a). Third, the effect of the finite temperature, e.g., appearing in the suppression factor $A(x)$ in Eq. (16a), is weakened, as the singlet-triplet splitting in QDR can be made much greater than the Zeeman splitting caused by a few millitesla magnetic field.

A challenging component of this alternative protocol may be to sufficiently reduce the exchange interaction J between the two spins, after they have been separated at the end of the initialization step. A nonzero exchange interaction strength introduces a nonzero singlet-triplet energy splitting in the two-particle spectrum, and hence a corresponding time scale \hbar/J , which poses an upper limit on the time scale $3N\tau_s$ of the N pumping cycles. That is, the condition $\frac{3N\tau_s J}{\hbar} \ll 1$ should be satisfied to neglect the effect of the residual exchange interaction. Substituting $\tau_s = 3$ ns and $N = 50$, we obtain the condition $J/\hbar \ll 2.3$ MHz.

D. Setups for proving the non-Abelian nature of the geometric quantum gate

A possible generalisation of the proposed measurement is to show that the induced geometric quantum gate in

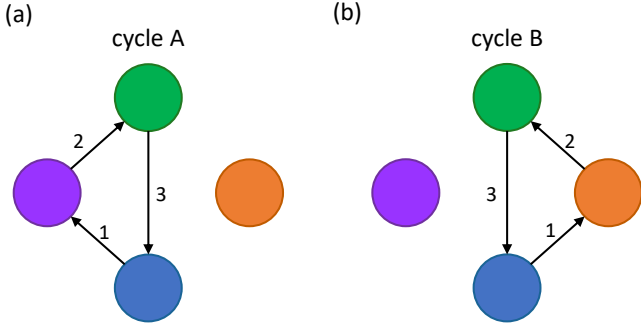


FIG. 8. Revealing the non-Abelian character of the geometric quantum gates. Panels (a) and (b) depict two different pumping cycles A and B in a 2×2 quantum dot array. In general, performing cycle A first and cycle B second leads to a different measurement result than shuttling in the reverse order.

a quantum dot loop is truly non-Abelian. One way to achieve this is by extending the loop in Fig. 1(a) with an additional quantum dot. Then the qubit can be driven through two different cycles after each other, as shown in Fig. 8(a) and (b). By showing that the induced transformation depends on the ordering of the different cycles, one can conclude that the geometric single-qubit gates induced by cycle A or cycle B do not commute.

The demonstration of the non-Abelian character of the geometric gate could also be attempted using three quantum dots only, by utilising nearby orbitals in QD2 and QD3. To discuss a simple example, we denote the charge configuration of the three dots as (N_1, N_2, N_3) , where N_j denotes the number of particles in QD j , counted with respect to a certain filled-shell configuration. Using this notation, the cycle QD1 \rightarrow QD2 \rightarrow QD3 \rightarrow QD1 studied so far corresponds to, e.g., $(1, 0, 0) \rightarrow (0, 1, 0) \rightarrow (0, 0, 1) \rightarrow (1, 0, 0)$; call this cycle A. A different cycle, say, cycle B, can be defined using the same three quantum dots by shifting the charge configuration of QD2 and QD3 such that the cycle takes the form $(1, 2, -2) \rightarrow (0, 3, -2) \rightarrow (0, 2, -1) \rightarrow (1, 2, -2)$. Since spin-orbit features, e.g., spin-dependent tunneling, is expected to vary between different shells [50], hence the non-Abelian Berry phase corresponding to cycle A and B are expected to be different, and in general, non-commuting.

E. Relation of our proposals to a recent ‘triangular shuttling’ experiment

In a recent experiment [58], coherent shuttling of a spin qubit through a quantum dot loop was demonstrated. In that manuscript, the ‘quantization axis tilt angles’ of tunnel-coupled quantum dot pairs were determined by spectroscopy, and also by using time-resolved shuttling experiments. Both experiments were carried out in a

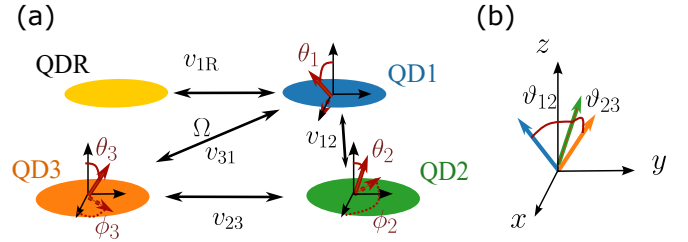


FIG. 9. Relation of the local Zeeman field directions and the quantization axis tilt angles. (a) Layout of the device used in Ref. [58]. Red solid vectors depict local Zeeman field directions $\mathbf{n}_1, \mathbf{n}_2, \mathbf{n}_3$. Labels on the tunnel couplings indicate the gauge choice: pseudospin-non-conserving tunneling (Ω) appears only on the bond between QD2 and QD3. (b) Quantization axis tilt angles ϑ_{12} and ϑ_{23} that were measured in Ref. [58]. Blue/green/orange arrow shows the local Zeeman field direction in QD1/QD2/QD3.

nonzero magnetic field with a fixed direction.

Here, we establish the relation between the quantization axis tilt angles and the parameters in our model. In Fig. 9(a), we draw the four-dot configuration used in [58]. In Fig. 9(a), we also indicate the gauge choice that is used in [58]: tunnel couplings between QDR \leftrightarrow QD1, QD1 \leftrightarrow QD2, and QD2 \leftrightarrow QD3 are transformed to be pseudospin-conserving, and the tunnel coupling between QD3 \leftrightarrow QD1 is retained as pseudospin-non-conserving. In this setting, the system of the three numbered QDs is described by the Hamiltonian in Eq. (10), with the only difference that in H_{stun} , the operator τ_{12}^y is replaced by τ_{23}^y .

In this gauge, at a finite magnetic field, the quantization axes of the numbered dots are given by the unit vectors \mathbf{n}_k , see below Eq. (10). We illustrate these quantization axes in Fig. 9(a), where the thick red arrows depict the vectors \mathbf{n}_k (arbitrary example), and the corresponding polar and azimuthal angles θ_k and ϕ_k are also indicated. The quantization axes \mathbf{n}_k are shown together in Fig. 9(b), where the angle enclosed by \mathbf{n}_1 and \mathbf{n}_2 is denoted by ϑ_{12} , and the angle enclosed by \mathbf{n}_2 and \mathbf{n}_3 is denoted by ϑ_{23} . These angles ϑ_{12} and ϑ_{23} were determined in the experiment [58]. The relation between these quantization axis tilt angles and the angle parameters of our Hamiltonian reads:

$$\vartheta_{jk} = \arccos(\cos(\phi_j - \phi_k) \sin \theta_j \sin \theta_k + \cos \theta_j \cos \theta_k), \quad (31)$$

where $jk \in \{12, 23\}$.

Note that the protocol we suggest in Sec. IV enables a more complete characterization of the Hamiltonian than the inference of the tilt angles; i.e., our protocol enables the inference of all five angle parameters $\theta_1, \theta_2, \phi_2, \theta_3, \phi_3$ (from these, the quantization axis tilt angles can be calculated using Eq. (31)), as well as the strength Ω of the pseudospin-non-conserving tunneling term.

The device and protocols used in Ref. [58] are very similar to those described in our present work, highlighting the near-term feasibility of our proposals. The device

of [58] has no on-chip pulsed magnetic field source, and utilizes Pauli blockade for initialisation and readout. As a consequence, it enables the direct implementation of our alternative protocol described in Sec. VC, and correspondingly, the inference of the angle of rotation of the holonomic quantum gate induced on the qubit by a single pumping cycle through the quantum dot loop. In fact, the ‘triangular shuttling’ protocol, which is carried out in a nonzero static magnetic field in Ref. [58], is identical to our alternative protocol (Sec. VC), if the magnetic field is switched off in the experiment.

Based on Ref. [58], we identify the slow diagonal shuttling (shuttling time of $\tau_s \approx 36$ ns) as a potential bottleneck to observe the oscillations predicted by Eq. (30). As we described above, the Earth’s magnetic field and hyperfine interaction set an upper bound on the time window of the experiment (presumably around one microsecond), and the qubit dynamics induced by the non-Abelian Berry phase may be masked by those magnetic effects if shuttling is too slow. Improvements are expected if the diagonal shuttling is sped up (e.g., by using a dedicated barrier gate addressing the corresponding tunnel barrier), by shielding the Earth’s magnetic field, and by using isotopically purified materials to suppress the hyperfine effect.

VI. CONCLUSION

We provided a theoretical description of the non-Abelian Berry phase or geometric quantum gate of a spin

qubit, induced upon an adiabatic shuttling cycle through a quantum-dot loop in the presence of spin-orbit interaction and absence of magnetic field. Time-reversal symmetry is expected to provide an extra level of protection of the Kramers degeneracy exploited in this setup, in contrast to earlier experiments where the degeneracy relies on fine-tuning of system parameters. We highlighted two experimental protocols to detect features of the non-Abelian Berry phase: the first (second) one relies on a pulsed magnetic field (zero-field Pauli spin blockade) for initialisation and readout. Furthermore, we predict that a variant of the first protocol can be used to infer the parameters of the spin-orbit-coupled Hamiltonian. We expect a near-term realisation of our protocol, as all key elements of it have been demonstrated in spin-qubit experiments. Such a realisation would be important to assess the potential of holonomic quantum gates for spin-based quantum information processing.

ACKNOWLEDGMENTS

We thank G. Fülöp, A. Geresdi, F. van Riggelen-Doelman, L. Vandersypen, and M. Veldhorst for useful discussions. This research was supported by the Ministry of Culture and Innovation and the National Research, Development and Innovation Office (NKFIH) within the Quantum Information National Laboratory of Hungary (Grant No. 2022-2.1.1-NL-2022-00004), by NKFIH via the OTKA Grant No. 132146, and by the European Union’s Horizon Europe research and innovation programme via the IGNITE project.

Appendix A: Gauge transformation in the three dot loop

In this appendix, we formulate the gauge transformation shown in Fig. 2, i.e. the transformation of the tunneling terms of the Hamiltonian from the form of Eq. (1) to Eq. (2). The tunneling terms of the Hamiltonian (1c) and (1d) in the block form expanded in the orbital degree of freedom reads as:

$$H_{\text{tun}} + H_{\text{stun}} = \begin{pmatrix} 0 & \tilde{v}_{12} - i\hbar\tilde{\Omega}_{12} \cdot \tilde{\sigma} & \tilde{v}_{31} + i\hbar\tilde{\Omega}_{31} \cdot \tilde{\sigma} \\ h.c. & 0 & \tilde{v}_{23} - i\hbar\tilde{\Omega}_{23} \cdot \tilde{\sigma} \\ h.c. & h.c. & 0 \end{pmatrix}, \quad (\text{A1})$$

where $\tilde{\sigma}$ are the Pauli matrices defined with the basis $(|\tilde{\uparrow}\rangle, |\tilde{\downarrow}\rangle)$. Let us first choose an appropriate basis in QD3 to eliminate the pseudospin-non-conserving tunneling between QD1 and QD3, that is, to eliminate $\tilde{\Omega}_{31}$ in Eq. (A1). We do this by choosing new local Kramers pairs to define the local Pauli operators; these new local Kramers pairs $|\hat{\uparrow}\rangle, |\hat{\downarrow}\rangle$ are chosen as

$$|k, \hat{\downarrow}\rangle = U_3 |k, \tilde{\downarrow}\rangle, |k, \hat{\uparrow}\rangle = U_3 |k, \tilde{\uparrow}\rangle, \quad (\text{A2})$$

where U_3 is a local pseudospin rotation in QD3 with rotation axis $\tilde{\omega}_{31} = \tilde{\Omega}_{31}/|\tilde{\Omega}_{31}|$ and angle $\tilde{\theta}_{\text{so}}^{(31)} = 2 \arctan \frac{\hbar|\tilde{\Omega}_{31}|}{\tilde{v}_{31}}$ in the clockwise (negative) direction. Explicitly, it reads:

$$U_3 = e^{-i\frac{\tilde{\theta}_{\text{so}}^{(31)}}{2}\tilde{\omega}_{31} \cdot \tilde{\sigma} \otimes \tau_3}. \quad (\text{A3})$$

Note that the Kramers basis states on QD1 and QD2 are unchanged by U_3 .

The Pauli operators in the new gauge, denoted as $\hat{\sigma}$, are related to the original Pauli operators $\tilde{\sigma}$ as

$$\hat{\sigma} \otimes \tau_k = U_3 (\tilde{\sigma} \otimes \tau_k) U_3^\dagger, \quad (\text{A4})$$

for all $k \in \{1, 2, 3\}$. Note that the unitary U_3 has the same form in the two gauges, i.e. $U_3 = e^{-i\frac{\tilde{\theta}_{\text{so}}^{(31)}}{2}\tilde{\omega}_{31}\cdot\tilde{\sigma}\otimes\tau_3} = e^{-i\frac{\tilde{\theta}_{\text{so}}^{(31)}}{2}\tilde{\omega}_{31}\cdot\hat{\sigma}\otimes\tau_3}$. Using this identity, the tunneling Hamiltonian in the new gauge reads as:

$$\begin{aligned} H_{\text{tun}} + H_{\text{stun}} &= \\ &= \begin{pmatrix} 0 & \tilde{v}_{12} - i\hbar\tilde{\Omega}_{12}\cdot\hat{\sigma} & (\tilde{v}_{31} + i\hbar\tilde{\Omega}_{31}\cdot\hat{\sigma})e^{-i\frac{\tilde{\theta}_{\text{so}}^{(31)}}{2}\tilde{\omega}_{31}\cdot\hat{\sigma}} \\ h.c. & 0 & (\tilde{v}_{23} - i\hbar\tilde{\Omega}_{23}\cdot\hat{\sigma})e^{-i\frac{\tilde{\theta}_{\text{so}}^{(31)}}{2}\tilde{\omega}_{31}\cdot\hat{\sigma}} \\ h.c. & h.c. & 0 \end{pmatrix} = \begin{pmatrix} 0 & \tilde{v}_{12} - i\hbar\tilde{\Omega}_{12}\cdot\hat{\sigma} & v_{31} \\ h.c. & 0 & \hat{v}_{23} - i\hbar\hat{\Omega}_{23}\cdot\hat{\sigma} \\ h.c. & h.c. & 0 \end{pmatrix}, \quad (\text{A5}) \end{aligned}$$

where we utilized the identity $e^{ian\cdot\sigma} = \cos(a) + i\sin(a)\mathbf{n}\cdot\sigma$, and introduced the parameters

$$v_{31} = \tilde{v}_{31} \cos\left(\frac{\tilde{\theta}_{\text{so}}^{(31)}}{2}\right) + \hbar|\tilde{\Omega}_{31}|\sin\left(\frac{\tilde{\theta}_{\text{so}}^{(31)}}{2}\right) = \sqrt{\tilde{v}_{31}^2 + \hbar^2|\tilde{\Omega}_{31}|^2}, \quad (\text{A6a})$$

$$\hat{v}_{23} = \tilde{v}_{23} \cos\left(\frac{\tilde{\theta}_{\text{so}}^{(31)}}{2}\right) - \hbar\tilde{\Omega}_{23}\cdot\tilde{\omega}_{31} \sin\left(\frac{\tilde{\theta}_{\text{so}}^{(31)}}{2}\right) = \frac{\tilde{v}_{23}\tilde{v}_{31} - \hbar^2\tilde{\Omega}_{23}\cdot\tilde{\Omega}_{31}}{\sqrt{\tilde{v}_{31}^2 + \hbar^2|\tilde{\Omega}_{31}|^2}}, \quad (\text{A6b})$$

$$\hat{\Omega}_{23} = \frac{1}{\hbar} \left((\tilde{v}_{23}\tilde{\omega}_{31} + \hbar\tilde{\Omega}_{23}\times\tilde{\omega}_{31}) \sin\left(\frac{\tilde{\theta}_{\text{so}}^{(31)}}{2}\right) + \hbar\tilde{\Omega}_{23} \cos\left(\frac{\tilde{\theta}_{\text{so}}^{(31)}}{2}\right) \right) = \frac{\tilde{v}_{31}\tilde{\Omega}_{23} + \tilde{v}_{23}\tilde{\Omega}_{31} + \hbar\tilde{\Omega}_{23}\times\tilde{\Omega}_{31}}{\sqrt{\tilde{v}_{31}^2 + \hbar^2|\tilde{\Omega}_{31}|^2}}. \quad (\text{A6c})$$

The pseudospin is indeed conserved upon tunneling between the third and the first dot in the new gauge, as v_{31} appearing in the top right block of the matrix on the right hand side of Eq. (A5) is a scalar.

Next, we eliminate the pseudospin-non-conserving tunneling between QD2 and QD3 with a rotation of the quantization axes on the second dot around $\hat{\omega}_{23} = \hat{\Omega}_{23}/|\hat{\Omega}_{23}|$ with an angle $\hat{\theta}_{\text{so}}^{(23)} = 2\arctan\frac{\hbar|\hat{\Omega}_{23}|}{\hat{v}_{23}}$ in the clockwise (negative) direction. The corresponding unitary transformation is $U_2 = e^{-i\frac{\hat{\theta}_{\text{so}}^{(23)}}{2}\hat{\omega}_{23}\cdot\hat{\sigma}\otimes\tau_2}$. We denote the new basis as:

$$|k, \uparrow\rangle = U_2 |k, \hat{\uparrow}\rangle, \quad |k, \downarrow\rangle = U_2 |k, \hat{\downarrow}\rangle, \quad (\text{A7})$$

similarly to the previous case. The transformation of the matrix form of the tunneling Hamiltonian is analogous to the previous one. This means that the tunneling between QD1 and QD3 remains invariant, the tunneling between QD2 and QD3 become pseudospin-conserving and the last tunneling term between QD1 and QD2 transforms non-trivially. Written out with the Pauli operators σ defined in the new gauge:

$$\begin{aligned} H_{\text{tun}} + H_{\text{stun}} &= \\ &= \begin{pmatrix} 0 & (\tilde{v}_{12} - i\hbar\tilde{\Omega}_{12}\cdot\sigma)e^{-i\frac{\hat{\theta}_{\text{so}}^{(23)}}{2}\hat{\omega}_{23}\cdot\sigma} & v_{31} \\ h.c. & 0 & e^{i\frac{\hat{\theta}_{\text{so}}^{(23)}}{2}\hat{\omega}_{23}\cdot\sigma}(\hat{v}_{23} - i\hbar\hat{\Omega}_{23}\cdot\sigma) \\ h.c. & h.c. & 0 \end{pmatrix} = \begin{pmatrix} 0 & v_{12} - i\hbar\Omega_{12}\cdot\sigma & v_{31} \\ h.c. & 0 & v_{23} \\ h.c. & h.c. & 0 \end{pmatrix}, \quad (\text{A8}) \end{aligned}$$

with the new parameters:

$$v_{12} = \tilde{v}_{12} \cos\left(\frac{\hat{\theta}_{\text{so}}^{(23)}}{2}\right) - \sin\left(\frac{\hat{\theta}_{\text{so}}^{(23)}}{2}\right) \hbar \tilde{\Omega}_{12} \cdot \hat{\omega}_{23} = \frac{\tilde{v}_{12} \hat{v}_{23} - \hbar^2 \tilde{\Omega}_{12} \cdot \hat{\Omega}_{23}}{\sqrt{\tilde{v}_{23}^2 + \hbar^2 |\tilde{\Omega}_{23}|^2}} =$$

$$= \frac{\tilde{v}_{12} \tilde{v}_{23} \tilde{v}_{31} - \tilde{v}_{12} \hbar^2 \tilde{\Omega}_{23} \cdot \tilde{\Omega}_{31} - \tilde{v}_{31} \hbar^2 \tilde{\Omega}_{12} \cdot \tilde{\Omega}_{23} - \tilde{v}_{23} \hbar^2 \tilde{\Omega}_{12} \cdot \tilde{\Omega}_{31} - \hbar^3 \tilde{\Omega}_{12} \cdot (\tilde{\Omega}_{23} \times \tilde{\Omega}_{31})}{\sqrt{(\tilde{v}_{23}^2 + \hbar^2 |\tilde{\Omega}_{23}|^2)(\tilde{v}_{31}^2 + \hbar^2 |\tilde{\Omega}_{31}|^2)}}, \quad (\text{A9a})$$

$$v_{23} = \tilde{v}_{12} \cos\left(\frac{\hat{\theta}_{\text{so}}^{(23)}}{2}\right) - \sin\left(\frac{\hat{\theta}_{\text{so}}^{(23)}}{2}\right) \hbar \tilde{\Omega}_{12} \cdot \hat{\omega}_{23} = \sqrt{\hat{v}_{23}^2 + \hbar^2 |\hat{\Omega}_{23}|^2} = \sqrt{\tilde{v}_{23}^2 + \hbar^2 |\tilde{\Omega}_{23}|^2}, \quad (\text{A9b})$$

$$\Omega_{12} = \frac{1}{\hbar} \left((\tilde{v}_{12} \hat{\omega}_{23} + \hbar \tilde{\Omega}_{12} \times \hat{\omega}_{23}) \sin\left(\frac{\hat{\theta}_{\text{so}}^{(23)}}{2}\right) + \cos\left(\frac{\hat{\theta}_{\text{so}}^{(23)}}{2}\right) \hbar \tilde{\Omega}_{12} \right) = \frac{\hat{v}_{23} \tilde{\Omega}_{12} + \tilde{v}_{12} \hat{\Omega}_{23} + \hbar \tilde{\Omega}_{12} \times \hat{\Omega}_{23}}{\sqrt{\tilde{v}_{23}^2 + \hbar^2 |\tilde{\Omega}_{23}|^2}} =$$

$$= \frac{\tilde{v}_{12} \tilde{v}_{23} \tilde{\Omega}_{31} + \tilde{v}_{31} \tilde{v}_{12} \tilde{\Omega}_{23} + \tilde{v}_{23} \tilde{v}_{31} \tilde{\Omega}_{12} + \tilde{v}_{12} (\hbar \tilde{\Omega}_{23} \times \tilde{\Omega}_{31}) + \tilde{v}_{23} (\hbar \tilde{\Omega}_{12} \times \tilde{\Omega}_{31}) + \tilde{v}_{31} (\hbar \tilde{\Omega}_{12} \times \tilde{\Omega}_{23})}{\sqrt{(\tilde{v}_{23}^2 + \hbar^2 |\tilde{\Omega}_{23}|^2)(\tilde{v}_{31}^2 + \hbar^2 |\tilde{\Omega}_{31}|^2)}} -$$

$$- \frac{\hbar^2 (\tilde{\Omega}_{23} \cdot \tilde{\Omega}_{31}) \tilde{\Omega}_{12} - (\tilde{\Omega}_{12} \cdot \tilde{\Omega}_{31}) \tilde{\Omega}_{23} + (\tilde{\Omega}_{12} \cdot \tilde{\Omega}_{23}) \tilde{\Omega}_{31}}{\sqrt{(\tilde{v}_{23}^2 + \hbar^2 |\tilde{\Omega}_{23}|^2)(\tilde{v}_{31}^2 + \hbar^2 |\tilde{\Omega}_{31}|^2)}}. \quad (\text{A9c})$$

To arrive to the form of Eq. (2), one needs to rotate the basis with a global pseudospin transformation to rotate the Ω_{12} vector to the z direction.

Appendix B: Gauge transformation of the Zeeman term

Let us calculate the effect of a local basis transformation on the Zeeman term of the Hamiltonian. The local Zeeman term of a dot can be written as

$$H_{\text{Zeeman}} = \frac{1}{2} \mu_B \tilde{\sigma} \cdot \tilde{g} B, \quad (\text{B1})$$

as given in Eq. (9). Consider the gauge transformation $U = e^{-i \frac{\theta_{\text{so}}}{2} \mathbf{n} \cdot \tilde{\sigma}}$, similar to the transformations in the previous appendix. Then, the Pauli operators defined with the new basis are related to the original ones by the formula

$$\tilde{\sigma} = U^\dagger \sigma U = \mathbf{R}_{\mathbf{n}}(\theta_{\text{so}}) \sigma, \quad (\text{B2})$$

where we introduced $\mathbf{R}_{\mathbf{n}}(\theta_{\text{so}})$ as a 3×3 rotation matrix around \mathbf{n} with angle θ_{so} . Then the Zeeman term expressed using the Pauli operators of the new basis is

$$H_{\text{Zeeman}} = \frac{1}{2} \mu_B (\mathbf{R}_{\mathbf{n}}(\theta_{\text{so}}) \sigma) \cdot \tilde{g} B = \frac{1}{2} \mu_B \sigma \cdot (\mathbf{R}_{\mathbf{n}}^{-1}(\theta_{\text{so}}) \tilde{g}) B = \frac{1}{2} \mu_B \sigma \cdot g B, \quad (\text{B3})$$

where we introduced the new g -tensor $g = \mathbf{R}_{\mathbf{n}}^{-1}(\theta_{\text{so}}) \tilde{g}$.

Using the above considerations, we express the local g -tensors of the three-dot loop after the gauge transformation considered in the previous appendix:

$$g_1 = \tilde{g}_1, \quad (\text{B4a})$$

$$g_2 = \mathbf{R}_{\tilde{\omega}_{23}}^{-1}(\hat{\theta}_{\text{so}}^{(23)}) \tilde{g}_2, \quad (\text{B4b})$$

$$g_3 = \mathbf{R}_{\tilde{\omega}_{31}}^{-1}(\hat{\theta}_{\text{so}}^{(31)}) \tilde{g}_3. \quad (\text{B4c})$$

Appendix C: Qubit readout error due to temperature broadening of the Fermi-Dirac distribution

The Elzerman readout scheme [16] for quantum-dot spin qubits relies on spin-to-charge conversion and subsequent charge readout. In this scheme, spin-to-charge conversion is enabled by a nearby reservoir of particles and energy-selective tunneling between the dot and the reservoir. In particular, the on-site energy of the dot is tuned such

that the chemical potential of the reservoir is in between the two Zeeman-split sublevels of the spin qubit, such that tunneling to the reservoir is suppressed (enhanced) for the ground (excited) state of the spin qubit. In turn, the absence or presence of the particle in the dot is measured by a sensitive charge sensor, e.g., a quantum point contact or a single-electron transistor.

The reservoir used for spin-to-charge conversion has a finite temperature, hence the Fermi-Dirac distribution of the particles in the reservoir is thermally broadened. This implies a nonzero readout error which we characterize in what follows. In particular, we ask the following question: if the spin qubit occupies the excited state with probability P_e right before readout, then what is the probability $P_e^{(m)}$ of the inference that it was in the excited state? The fact that $P_e \neq P_e^{(m)}$ (see below) is interpreted as a thermally induced readout error, and it influences the contrast of the oscillations described in Secs. III and IV.

In our model, we define the excited-state inference probability $P_e^{(m)}$ as the probability that the particle has left the dot at least once during the charge sensing measurement. We consider the case when charge sensing is done such that the chemical potential of the reservoir aligns with the average energy of the two Zeeman sublevels of the spin qubit. To describe the tunneling events, we introduce the tunneling-out rates as

$$\Gamma_g = \Gamma(1 - f(\mu - \hbar\omega/2)), \quad (C1)$$

$$\Gamma_e = \Gamma(1 - f(\mu + \hbar\omega/2)), \quad (C2)$$

where Γ is the bare tunneling amplitude between the dot and the reservoir, f is the Fermi-Dirac distribution and $\hbar\omega$ is the splitting between the excited state and the ground state.

Let us assume, that the system is in the excited (ground) state. Then the probability that it has not tunneled out after time τ_r is $e^{-\Gamma_e\tau_r}$ ($e^{-\Gamma_g\tau_r}$). Thus, the probability of jumping out from the excited (ground) state is $1 - e^{-\Gamma_e\tau_r}$ ($1 - e^{-\Gamma_g\tau_r}$). Therefore, the inferred excited-state probability reads as

$$P_e^{(m)}(P_e, \tau_r) = (1 - e^{-\Gamma_e\tau_r})P_e + (1 - P_e)(1 - e^{-\Gamma_g\tau_r}) = (e^{-\Gamma_g\tau_r} - e^{-\Gamma_e\tau_r})P_e + (1 - e^{-\Gamma_g\tau_r}). \quad (C3)$$

This implies that the contrast of the signal obtained from many Elzerman-type measurement runs is reduced by the factor

$$\tilde{A}(\omega, T, \Gamma, \tau_r) = e^{-\Gamma_g\tau_r} - e^{-\Gamma_e\tau_r}. \quad (C4)$$

To maximize the contrast at a given magnetic field, temperature, and tunneling rate, this factor \tilde{A} should be maximized over the readout time τ_r . This yields a maximal contrast at an optimal readout time of

$$\tau_r^* = \frac{\ln(\Gamma_e/\Gamma_g)}{\Gamma_e - \Gamma_g}. \quad (C5)$$

In this optimized setting, the contrast reduction factor reads:

$$\begin{aligned} A\left(\frac{\hbar\omega}{2k_B T}\right) &= \tilde{A}(\omega, T, \Gamma, \tau_r^*) = \exp\left(\frac{-\Gamma_g \ln(\Gamma_e/\Gamma_g)}{\Gamma_e - \Gamma_g}\right) - \exp\left(\frac{-\Gamma_e \ln(\Gamma_e/\Gamma_g)}{\Gamma_e - \Gamma_g}\right) = \\ &= \exp\left(-\frac{\frac{\hbar\omega}{2k_B T}}{e^{\frac{\hbar\omega}{2k_B T}} - 1}\right) - \exp\left(-\frac{\frac{\hbar\omega}{2k_B T}}{1 - e^{-\frac{\hbar\omega}{2k_B T}}}\right). \end{aligned} \quad (C6)$$

Note that the maximum value does not depend on the tunneling amplitude Γ .

-
- [1] N. W. Hendrickx, W. I. Lawrie, M. Russ, F. van Riggelen, S. L. de Snoo, R. N. Schouten, A. Sammak, G. Scappucci, and M. Veldhorst, A four-qubit germanium quantum processor, *Nature* **591**, 580 (2021).
- [2] N. W. Hendrickx, L. Massai, M. Mergenthaler, F. Schupp, S. Paredes, S. W. Bedell, G. Salis, and A. Fuhrer, Sweet-spot operation of a germanium hole spin qubit with highly anisotropic noise sensitivity (2023), arXiv:2305.13150 [cond-mat.mes-hall].
- [3] M. T. Mądzik, S. Asaad, A. Youssry, B. Joecker, K. M.

- Rudinger, E. Nielsen, K. C. Young, T. J. Proctor, A. D. Baczewski, A. Laucht, V. Schmitt, F. E. Hudson, K. M. Itoh, A. M. Jakob, B. C. Johnson, D. N. Jamieson, A. S. Dzurak, C. Ferrie, R. Blume-Kohout, and A. Morello, Precision tomography of a three-qubit donor quantum processor in silicon, *Nature* **601**, 348 (2022).
- [4] A. Noiri, K. Takeda, T. Nakajima, T. Kobayashi, A. Sammak, G. Scappucci, and S. Tarucha, Fast universal quantum gate above the fault-tolerance threshold in silicon, *Nature* **601**, 338 (2022).

- [5] X. Xue, M. Russ, N. Samkharadze, B. Undseth, A. Sammak, G. Scappucci, and L. M. K. Vandersypen, Quantum logic with spin qubits crossing the surface code threshold, *Nature* **601**, 343 (2022).
- [6] S. G. J. Philips, M. T. Mađzik, S. V. Amitonov, S. L. de Snoo, M. Russ, N. Kalhor, C. Volk, W. I. L. Lawrie, D. Brousse, L. Tryputen, B. P. Wuetz, A. Sammak, M. Veldhorst, G. Scappucci, and L. M. K. Vandersypen, Universal control of a six-qubit quantum processor in silicon, *Nature* **609**, 919 (2022).
- [7] V. N. Golovach, M. Borhani, and D. Loss, Electric-dipole-induced spin resonance in quantum dots, *Physical Review B* **74**, 165319 (2006).
- [8] K. C. Nowack, F. H. L. Koppens, Y. V. Nazarov, and L. M. K. Vandersypen, Coherent Control of a Single Electron Spin with Electric Fields, *Science* **318**, 1430 (2007).
- [9] A. Crippa, R. Maurand, L. Bourdet, D. Kotekar-Patil, A. Amisse, X. Jehl, M. Sanquer, R. Laviéville, H. Bohuslavskyi, L. Hutin, S. Barraud, M. Vinet, Y.-M. Niquet, and S. De Franceschi, Electrical spin driving by g-matrix modulation in spin-orbit qubits, *Physical Review Letters* **120**, 137702 (2018).
- [10] F. Wilczek and A. Zee, Appearance of Gauge Structure in Simple Dynamical Systems, *Physical Review Letters* **52**, 2111 (1984).
- [11] V. N. Golovach, M. Borhani, and D. Loss, Holonomic quantum computation with electron spins in quantum dots, *Physical Review A* **81**, 022315 (2010).
- [12] P. San-Jose, B. Scharfenberger, G. Schön, A. Shnirman, and G. Zarand, Geometric phases in semiconductor spin qubits: Manipulations and decoherence, *Physical Review B* **77**, 045305 (2008).
- [13] S. Prem, M. M. Wysokiński, and M. Trif, Longitudinal coupling between electrically driven spin-qubits and a resonator (2023), arXiv:2301.10163 [cond-mat.mes-hall].
- [14] P. Zanardi and M. Rasetti, Holonomic quantum computation, *Physics Letters A* **264**, 94 (1999).
- [15] P. San-Jose, G. Zarand, A. Shnirman, and G. Schön, Geometrical Spin Dephasing in Quantum Dots, *Physical Review Letters* **97**, 076803 (2006).
- [16] J. M. Elzerman, R. Hanson, L. H. Willems van Beveren, B. Witkamp, L. M. K. Vandersypen, and L. P. Kouwenhoven, Single-shot read-out of an individual electron spin in a quantum dot, *Nature* **430**, 431 (2004).
- [17] M. V. Berry, Quantal phase factors accompanying adiabatic changes, *Proceedings of the Royal Society of London. A. Mathematical and Physical Sciences* **392**, 45 (1984).
- [18] A. Tomita and R. Y. Chiao, Observation of Berry's Topological Phase by Use of an Optical Fiber, *Physical Review Letters* **57**, 937 (1986).
- [19] B. Grbić, R. Leturcq, T. Ihn, K. Ensslin, D. Reuter, and A. D. Wieck, Aharonov-Bohm Oscillations in the Presence of Strong Spin-Orbit Interactions, *Physical Review Letters* **99**, 176803 (2007).
- [20] F. Nagasawa, D. Frustaglia, H. Saarikoski, K. Richter, and J. Nitta, Control of the spin geometric phase in semiconductor quantum rings, *Nature Communications* **4**, 2526 (2013).
- [21] J.-B. Yau, E. P. De Poortere, and M. Shayegan, Aharonov-Bohm Oscillations with Spin: Evidence for Berry's Phase, *Physical Review Letters* **88**, 146801 (2002).
- [22] Y. J. Lin, R. L. Compton, K. Jiménez-García, J. V. Porto, and I. B. Spielman, Synthetic magnetic fields for ultracold neutral atoms, *Nature* **462**, 628 (2009).
- [23] P. J. Leek, J. M. Fink, A. Blais, R. Bianchetti, M. Göppl, J. M. Gambetta, D. I. Schuster, L. Frunzio, R. J. Schoelkopf, and A. Wallraff, Observation of Berry's Phase in a Solid-State Qubit, *Science* **318**, 1889 (2007).
- [24] S. Berger, M. Pechal, P. Kurpiers, A. A. Abdumalikov, C. Eichler, J. A. Mlynek, A. Shnirman, Y. Gefen, A. Wallraff, and S. Filipp, Measurement of geometric dephasing using a superconducting qubit, *Nature Communications* **6**, 8757 (2015).
- [25] J. W. Zwanziger, M. Koenig, and A. Pines, Non-Abelian effects in a quadrupole system rotating around two axes, *Physical Review A* **42**, 3107 (1990).
- [26] T. Li, L. A. Yeoh, A. Srinivasan, O. Klochan, D. A. Ritchie, M. Y. Simmons, O. P. Sushkov, and A. R. Hamilton, Manifestation of a non-Abelian Berry phase in a p-type semiconductor system, *Physical Review B* **93**, 205424 (2016).
- [27] S. Sugawa, F. Salces-Carcoba, Y. Yue, A. Putra, and I. B. Spielman, Wilson loop and Wilczek-Zee phase from a non-Abelian gauge field, *npj Quantum Information* **7**, 144 (2021).
- [28] Q.-X. Lv, H.-Z. Liu, Y.-X. Du, L.-Q. Chen, M. Wang, J.-H. Liang, Z.-X. Fu, Z.-Y. Chen, H. Yan, and S.-L. Zhu, Measurement of non-abelian gauge fields using multi-loop amplification (2023), arXiv:2305.05849 [quant-ph].
- [29] M. Kremer, L. Teuber, A. Szameit, and S. Scheel, Optimal design strategy for non-Abelian geometric phases using Abelian gauge fields based on quantum metric, *Physical Review Research* **1**, 033117 (2019).
- [30] Y. Yang, C. Peng, D. Zhu, H. Buljan, J. D. Joannopoulos, B. Zhen, and M. Soljačić, Synthesis and observation of non-Abelian gauge fields in real space, *Science* **365**, 1021 (2019).
- [31] F. Borsoi, N. W. Hendrickx, V. John, S. Motz, F. van Riggelen, A. Sammak, S. L. de Snoo, G. Scappucci, and M. Veldhorst, Shared control of a 16 semiconductor quantum dot crossbar array (2022), arXiv:2209.06609 [cond-mat.mes-hall].
- [32] F. van Riggelen, W. I. L. Lawrie, M. Russ, N. W. Hendrickx, A. Sammak, M. Rispler, B. M. Terhal, G. Scappucci, and M. Veldhorst, Phase flip code with semiconductor spin qubits, *npj Quantum Information* **8**, 124 (2022).
- [33] C.-A. Wang, C. Déprez, H. Tidjani, W. I. L. Lawrie, N. W. Hendrickx, A. Sammak, G. Scappucci, and M. Veldhorst, Probing resonating valence bonds on a programmable germanium quantum simulator (2022), arXiv:2208.11505 [quant-ph].
- [34] H. Flentje, P.-A. Mortemousque, R. Thalineau, A. Ludwig, A. D. Wieck, C. Bäuerle, and T. Meunier, Coherent long-distance displacement of individual electron spins, *Nature Communications* **8**, 501 (2017).
- [35] P.-A. Mortemousque, B. Jadot, E. Chanrion, V. Thiney, C. Bäuerle, A. Ludwig, A. D. Wieck, M. Urdampilleta, and T. Meunier, Enhanced Spin Coherence while Displacing Electron in a Two-Dimensional Array of Quantum Dots, *PRX Quantum* **2**, 030331 (2021).
- [36] J. Danon and Y. V. Nazarov, Pauli spin blockade in the presence of strong spin-orbit coupling, *Physical Review B* **80**, 041301 (2009).
- [37] F. H. L. Koppens, C. Buizert, K. J. Tielrooij, I. T. Vink, K. C. Nowack, T. Meunier, L. P. Kouwenhoven, and

- L. M. K. Vandersypen, Driven coherent oscillations of a single electron spin in a quantum dot, *Nature* **442**, 766 (2006).
- [38] J. J. Pla, K. Y. Tan, J. P. Dehollain, W. H. Lim, J. J. Morton, F. A. Zwanenburg, D. N. Jamieson, A. S. Dzurak, and A. Morello, High-fidelity readout and control of a nuclear spin qubit in silicon, *Nature* **496**, 334 (2013).
- [39] C. Zener, Non-adiabatic crossing of energy levels, *Proceedings of the Royal Society of London. Series A, Containing Papers of a Mathematical and Physical Character* **137**, 696 (1932).
- [40] J. Fischer, W. A. Coish, D. V. Bulaev, and D. Loss, Spin decoherence of a heavy hole coupled to nuclear spins in a quantum dot, *Physical Review B* **78**, 155329 (2008).
- [41] P. Philippopoulos, *Hyperfine and spin-orbit interactions in semiconductor nanostructures*, Ph.D. thesis, McGill University, Montreal (2020).
- [42] J. A. Krzywda and L. Cywiński, Adiabatic electron charge transfer between two quantum dots in presence of $1/f$ noise, *Physical Review B* **101**, 035303 (2020).
- [43] J. A. Krzywda and L. Cywiński, Interplay of charge noise and coupling to phonons in adiabatic electron transfer between quantum dots, *Physical Review B* **104**, 075439 (2021).
- [44] R. Winkler, *Spin—Orbit Coupling Effects in Two-Dimensional Electron and Hole Systems*, Vol. 191 (Springer Berlin Heidelberg, Berlin, Heidelberg, 2003).
- [45] D. Jirovec, A. Hofmann, A. Ballabio, P. M. Mutter, G. Tavani, M. Botifoll, A. Crippa, J. Kukucka, O. Sagi, F. Martins, J. Saez-Mollejo, I. Prieto, M. Borovkov, J. Arbiol, D. Chrastina, G. Isella, and G. Katsaros, A singlet-triplet hole spin qubit in planar Ge, *Nature Materials* **20**, 1106 (2021).
- [46] J. Krieger, *Design of a superconducting magnetic shield An experimental semester thesis performed at the Quantum Device Laboratory*, Ph.D. thesis, ETH Zürich, Zürich (2014).
- [47] J. M. Kreikebaum, A. Dove, W. Livingston, E. Kim, and I. Siddiqi, Optimization of infrared and magnetic shielding of superconducting TiN and Al coplanar microwave resonators, *Superconductor Science and Technology* **29**, 104002 (2016).
- [48] D. Flanigan, B. R. Johnson, M. H. Abitbol, S. Bryan, R. Cantor, P. Day, G. Jones, P. Mauskopf, H. McCarrick, A. Miller, and J. Zmuidzinas, Magnetic field dependence of the internal quality factor and noise performance of lumped-element kinetic inductance detectors, *Applied Physics Letters* **109**, 143503 (2016).
- [49] R. T. Gordon, C. E. Murray, C. Kurter, M. Sandberg, S. A. Hall, K. Balakrishnan, R. Shelby, B. Wacaser, A. A. Stabile, J. W. Sleight, M. Brink, M. B. Rothwell, K. P. Rodbell, O. Dial, and M. Steffen, Environmental radiation impact on lifetimes and quasiparticle tunneling rates of fixed-frequency transmon qubits, *Applied Physics Letters* **120**, 074002 (2022).
- [50] L. Han, M. Chan, D. de Jong, C. Prosko, G. Badawy, S. Gazibegovic, E. P. Bakkers, L. P. Kouwenhoven, F. K. Malinowski, and W. Pfaff, Variable and Orbital-Dependent Spin-Orbit Field Orientations in an InSb Double Quantum Dot Characterized via Dispersive Gate Sensing, *Physical Review Applied* **19**, 014063 (2023).
- [51] J. C. Abadillo-Uriel, E. A. Rodríguez-Mena, B. Martínez, and Y.-M. Niquet, Hole spin driving by strain-induced spin-orbit interactions (2022), arXiv:2212.03691 [cond-mat.mes-hall].
- [52] B. Martínez, J. C. Abadillo-Uriel, E. A. Rodríguez-Mena, and Y.-M. Niquet, Hole spin manipulation in inhomogeneous and nonseparable electric fields, *Physical Review B* **106**, 235426 (2022).
- [53] J. Huang, J. S. Xia, D. C. Tsui, L. N. Pfeiffer, and K. W. West, Disappearance of Metal-Like Behavior in GaAs Two-Dimensional Holes below 30 mK, *Physical Review Letters* **98**, 226801 (2007).
- [54] D. Maradan, L. Casparis, T.-M. Liu, D. E. F. Biesinger, C. P. Scheller, D. M. Zumbühl, J. D. Zimmerman, and A. C. Gossard, GaAs Quantum Dot Thermometry Using Direct Transport and Charge Sensing, *Journal of Low Temperature Physics* **175**, 784 (2014).
- [55] M. Sarsby, N. Yurttagül, and A. Geresdi, 500 microkelvin nanoelectronics, *Nature Communications* **11**, 1492 (2020).
- [56] M. Samani, C. P. Scheller, O. S. Sedeh, D. M. Zumbühl, N. Yurttagül, K. Grigoras, D. Gunnarsson, M. Prunnila, A. T. Jones, J. R. Prance, and R. P. Haley, Microkelvin electronics on a pulse-tube cryostat with a gate Coulomb-blockade thermometer, *Physical Review Research* **4**, 033225 (2022).
- [57] J. R. Petta, A. C. Johnson, J. M. Taylor, E. A. Laird, A. Yacoby, M. D. Lukin, C. M. Marcus, M. P. Hanson, and A. C. Gossard, Applied physics: Coherent manipulation of coupled electron spins in semiconductor quantum dots, *Science* **309**, 2180 (2005).
- [58] F. van Riggelen-Doelman, C.-A. Wang, S. L. de Snoo, W. I. L. Lawrie, N. W. Hendrickx, M. Rimbach-Russ, A. Sammak, G. Scappucci, C. Déprez, and M. Veldhorst, Coherent spin qubit shuttling through germanium quantum dots (2023), arXiv:2308.02406 [cond-mat.mes-hall].